Computational fluid dynamics study of unconventional air vehicle configurations

R. Ramamurti and W. Sandberg
Laboratory for Computational Physics and Fluid Dynamics, Naval Research Laboratory
Washington DC, USA

P. Vaiana,
The Pennsylvania State University
Pennsylvania, USA

J. Kellogg
Tactical Electronic Warfare Division,
Naval Research Laboratory,
Washington DC, USA

D. Cylinder
Princeton Plasma Physics Laboratory
Princeton University
New Jersey, USA

ABSTRACT

Two unconventional micro air vehicles developed by the Naval Research Laboratory are described. One of the vehicles employs flapping wings which is inspired by the flight of birds or insects but does not copy it directly. The second vehicle is a stop-rotor hybrid vehicle employing a pair of single blade, rotary/fixed wing panels, attached at their roots to separate coaxial shafts. An unstructured grid based incompressible flow solver, called *feflo*, is used to simulate the flow past these novel configurations in order to determine the flight characteristics of these vehicles.

1.0 INTRODUCTION

The Naval Research Laboratory (NRL) is developing a group of micro air vehicle (MAV) intended to perform in the low Reynolds number (< 50,000) regime. In this regime, the performance of the propeller decreases as the size decreases. Flapping wings can be advantageous under these conditions. While many flapping wing vehicles such as ornithopters attempt to mimic the flight of birds or insects, it is possible to use flapping foil propulsion in ways that are inspired by biological flight but do not copy it directly. Three configurations have flown successfully: a vehicle with a fixed forward wing and a rear flapping wing; a tandem fixed-wing design with a third flapping wing that claps down atop the rear fixed surface on each stroke; and a vehicle with tandem pairs of biplane configured flapping wings, in which each pair moves in opposition so as to alternately clap together and separate. This latter vehicle, which does not employ fixed lifting surfaces, has the advantage of being dynamically balanced in flight so that its center of mass is not forced to oscillate vertically by the flapping action. In addition, development is underway on a stop-rotor hybrid vehicle. This employs a pair of single-blade, rotary/fixed wing panels, attached at their roots to separate coaxial shafts. For low-speed flight the wing panels are driven as contra-rotating rotor blades for lift. A pusher propeller provides primary thrust, and control surfaces in the propeller wash provide pitch, yaw, and roll control. In fixed wing flight the wing panels are stopped opposite each other to become a conventional wing. This configuration eliminates the airflow reversal over the wing that occurs upon conversion in other stop-rotor designs. Developmental models of this vehicle have flown successfully in both fixed and rotary wing modes. Computational fluid dynamics (CFD) studies of these vehicles are performed using an unstructured grid based finite element incompressible flow solver called, *feflo*, to optimise propulsion efficiency and flight control techniques. In this paper, description of the flow solver and adaptive remeshing, descriptions of the flying models, CFD simulation results of two novel unmanned air vehicles will be presented.

Paper No. 2902. Manuscript received 22 July 2004, revised version received 24 March 2005, accepted 13 April 2005
Presented at the 19th Bristol International Conference on Unmanned Air Vehicle Systems, Bristol, UK, 29-31 March, 2004.

https://doi.org/10.1017/S0001924000000786 Published online by Cambridge University Press

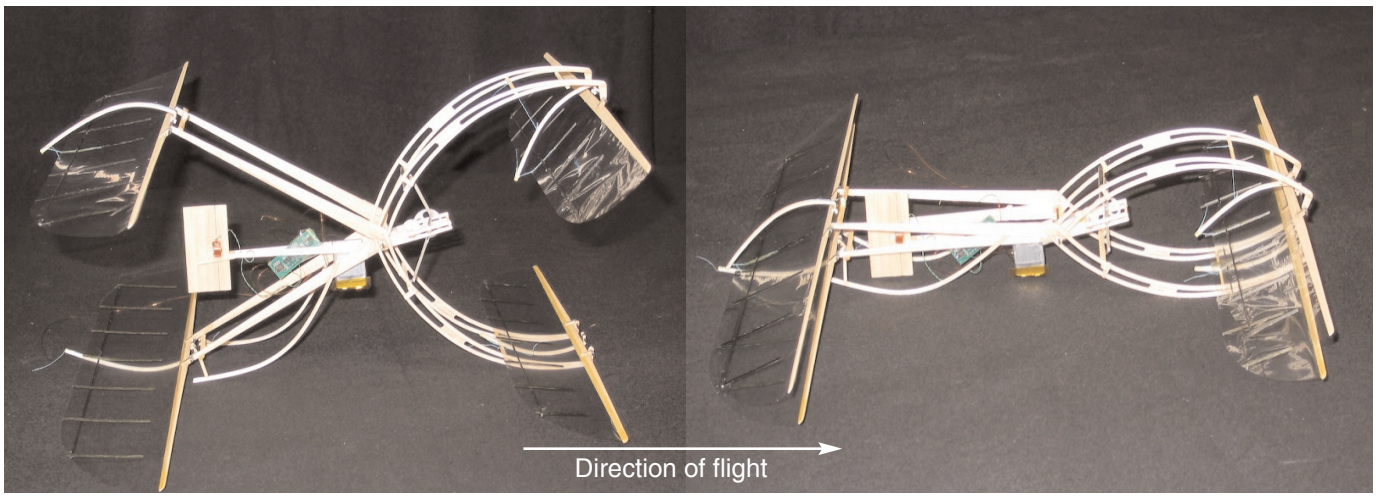


Figure 1. A radio controlled BITE-wing vehicle with foils separated shown in the left view and in the clapping position shown in the right view.

2.0 THE INCOMPRESSIBLE FLOW SOLVER

The governing equations employed are the incompressible Navier-Stokes equations in Arbitrary Lagrangian-Eulerian (ALE) formulation which are written as,

$$\frac{\mathrm{d}\mathrm{v}}{\mathrm{d}t} + \mathrm{v}_a \cdot \nabla \mathrm{v} + \nabla p = \nabla \cdot \sigma \qquad \ldots (1)$$

$$\nabla \cdot \mathrm{v} = 0 \qquad \ldots (2)$$

where p denotes the pressure, $\mathrm{v}_a = \mathrm{v} - \mathrm{w}$ the advective velocity vector, where v is the flow velocity and w is the mesh velocity and the material derivative is with respect to the mesh velocity w. Both the pressure p and the stress tensor σ have been normalised by the (constant) density ρ and are discretised in time using an implicit time stepping procedure. Thus the equations are Eulerian for zero mesh velocity and Lagrangian if the mesh velocity is the same as the flow velocity. The present time-accurate flow solver is discretised in space using a Galerkin procedure with linear tetrahedral elements. The unknowns are advanced in time using a projection method. Thus, the velocities are updated first. The predicted velocity field is then projected into a divergence-free field by solving a Poisson-type equation for pressure. The large linear system of equations that appear in this step is solved using a preconditioned conjugate gradient algorithm. The inflow boundary conditions for the computation are prescribed velocity while pressure is prescribed as the outflow boundary. The far field boundary conditions are slip velocity conditions and for viscous cases no-slip boundary conditions are prescribed on the body. The flow is initialised with uniform flow in the entire domain except on the surface of the body where no-slip conditions are prescribed. The details of the flow solver have already been discussed extensively elsewhere (Ramamurti *et al*, 1992, 1995)[6-10] in connection with successfully validated solutions for numerous 2D and 3D, laminar and turbulent, steady and unsteady flow problems.

3.0 RIGID/FLAPPING BODY MOTION AND ADAPTIVE REMESHING

In order to fully couple the motion of rigid bodies with the hydrodynamic or aerodynamic forces exerted on them, consistent rigid body motion integrators must be developed. The governing equations of motion for rigid bodies are well known. In the present work, the pressure distribution on the surface is integrated to compute forces and moments at each time step and the equations of motion are advanced in time to produce self-consistent trajectories. A more detailed description of the equations and the incorporation of the rigid body motion in the numerical scheme for solving the fluid flow are described in Ramamurti *et al* (1994)[7].

In order to carry out computations of the flow about oscillating and deforming geometries one needs to describe grid motion on a moving surface, couple the moving surface grid to the volume grid. The volume grid in the proximity of the moving surface is then remeshed, to eliminate badly distorted elements. A representative application requiring these gridding capabilities is the computation of the flow about pitching and heaving airfoils and the computation of vorticity shedding from the edges of oscillating foils. It is also essential for computing the flow past objects which are both accelerating and deforming. In deformations, the surface motion may be severe, leading, in the absence of remeshing, to distorted elements which in turn lead to poor numerical results. If the bodies in the flow field undergo arbitrary movement, a fixed mesh structure will lead to badly distorted elements. This means that at least a partial regeneration of the computational domain is required. On the other hand, if the bodies move through the flow field, the positions of relevant flow features will change. Therefore, in most of the computational domain a new mesh distribution will be required. Several mesh movement algorithms were developed in order to reduce the number of remeshings required throughout the unsteady flow simulation and are given in detail by Ramamurti and Sandberg (2002)[9].

2.1 Mesh movement from prescribed surface motion

The ability to move the mesh based on the kinematics of a continuously deforming surface opens the possibility to study actuators, compliant surface devices and animal locomotion in water and air. Such a capability was implemented in *feflo*. The user prescribes, with tables, the motion of surface geometry in time. The code then identifies the parametric coordinates ξ, η of each surface point. While ξ, η are kept constant during the simulation for surface points, their Cartesian coordinates (x,y,z) change in time according to the prescribed motion.

https://doi.org/10.1017/S0001924000000786 Published online by Cambridge University Press

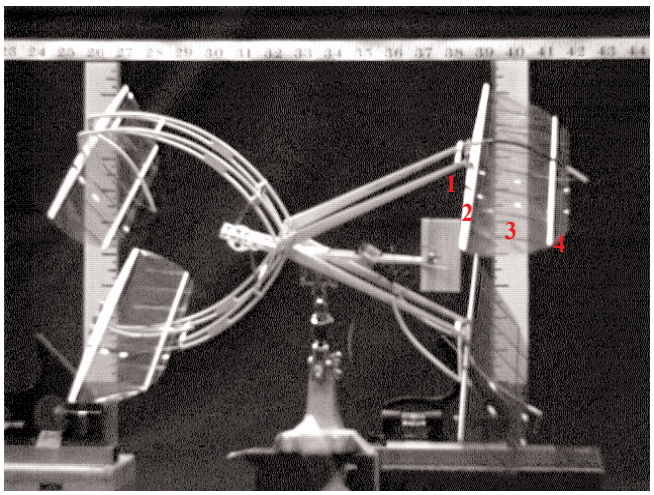


Figure 2. Setup of the BITE vehicle showing the luminescent markers.

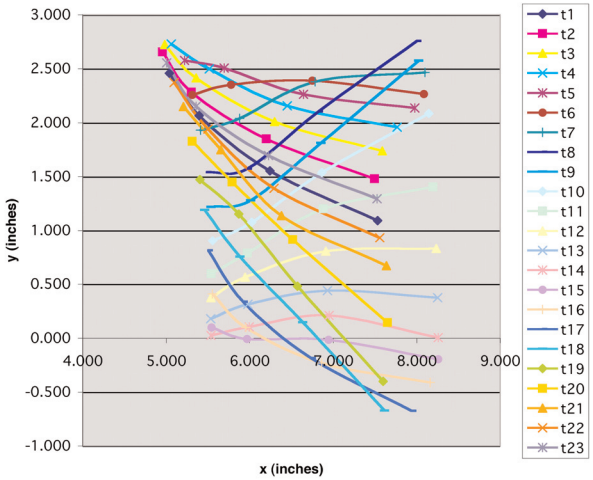


Figure 3. Cross sectional shape of the top of the rear pair of wings at various times through a flapping cycle.

3.0 BIOMORPHIC FLIGHT

While many flapping wing vehicles, such as ornithopters, tend to directly mimic the flight and control of birds or insects, it is possible to use flapping foil principles in ways that are inspired by biological flight mechanisms, but do not copy them directly-so-called 'biomorphic' flying configurations. For example, 'aerial swimming' vehicles can use a single, reversing-camber flapping wing at the rear, in contrast to a set of normal biological wings. Two other biomorphic configurations, to be treated in some detail later, are the clapping reversing-camber airfoil which creates and makes use of pressure pulses to augment thrust, and the tandem pair of clapping reversing camber-airfoils which provide both thrust and lift. Detailed description of our initial configurations such as the reversing camber *Delphinopter* and the clapping reversing camber *Pectenopter* is given by Kellogg *et al* (2003)[5].

Such biomorphic configurations offer the possibility of configurations that are not found in nature at all, or are 'unnatural' combinations of natural flight mechanisms. In addition, this approach invites the exploitation of mechanical, structural and chemical technologies not found in nature, but potentially useful toward our particular MAV objectives: rotating machinery, electric motors, and composite materials to name a few.

We have also ventured into novel MAV configurations that are more bio-inspired than biomorphic. The grasshopper-like Samara, for example, a stop-rotor hybrid rotary/fixed wing vehicle was conceived to provide effective mobility, including hovering and high-speed capabilities.

3.1 Tandem clapping foils: BITE-Wing

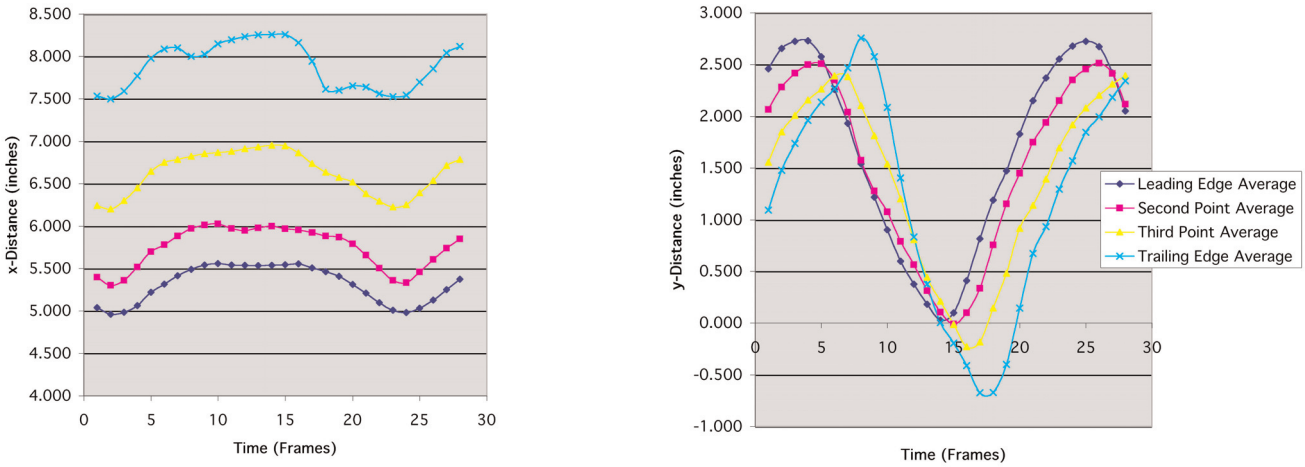
Our initial flapping airfoil configurations were hybrid fixed/flapping wing vehicles in that they each had fixed wing surfaces that provided most of the lift necessary for sustained flight. Birds and insects in general do not have substantial fixed lifting surfaces unrelated to propulsion and control. To approach more closely this biological feature and its potential advantages, another configuration was developed that has no fixed lifting surfaces and uses two tandem sets of clapping pairs of reversing camber wings for both thrust and lift. The biplane insectoid travel engine (BITE-Wing) shown in Fig. 1 employs several mechanisms common to insect locomotion for both flight and ground mobility.

The wing support structure is a pair of mirror-image beams with a central hinge point, resembling a pair of tongs. The clapping wing pairs are located at the extremities of both beams. This configuration has the advantage of being dynamically balanced, so that the vehicle's center of mass is not driven in a vertical oscillation by the flapping motion. A small central fuselage contains the control circuitry, energy store, the drive system by which the beams are flapped, and, in the current version, supports a conventional aerodynamic rudder. Each clapping foil uses the reversing camber mechanism. In order to provide appropriate lift and forward thrust for sustained flight, each flexible foil is hinged at the spanwise center of its leading edge and restricted in up and down motion such that airflow is directed both rearward and downward. The test vehicle is powered by a 4-watt electric motor, geared to provide 8-10Hz oscillation of the beams at cruise speed. A 3·6 gram lithium-ion polymer cell supplies electrical power. For the initial flights, a micro radio control system provides motor speed control and rudder for yaw control. Pitch and altitude control is achieved through motor power. Total weight is 19·5 grams. Early flight tests achieved stable, slow and controllable flights. By pitching the vehicle nose upward, it has demonstrated sufficient thrust for hovering. The oscillating beam members also make it possible for the vehicle to crawl, inchworm fashion, along the ground, as well as rise off the ground from a standstill and transition into full flight.

The reversing camber flapping foils originally developed by Cylinder and described by Kellogg *et al* (2001)[4] were reported by Jones and Platzer (2003)[3] to undergo aeroelastic deformation at flapping frequencies above 10Hz. This was confirmed in the BITE-Wing, in which the electric drive system permitted higher flapping frequencies than in previous rubber powered vehicles. The addition of a thin transverse stiffener toward the trailing edge of the reversing camber foils solved this problem, and no deformation could be observed at its maximum operating frequency.

The BITE-Wing made its first flights in January 2003. Work is currently focused on improving flight trim and control by differential motion of one or more of the flapping surfaces. This should eliminate the need for the conventional rudder and allow control in hover at zero airspeed. In addition, computational fluid dynamics (CFD) studies are underway to achieve a better understanding of the action of the reversing-camber flapping foils, the effects of their clapping together, and interaction between the front and rear pairs of wings. The latter of these raises the possibility that a vortex produced by the leading pair might be captured by a subsequent stroke of the rear pair. This mechanism of vortex capture is fundamental to increased efficiency in insect flight. The next section will cover the results of our CFD simulations thus far.

https://doi.org/10.1017/S0001924000000786 Published online by Cambridge University Press



(a) *x*-co-ordinate (b) *y*-co-ordinate

Figure 4. Kinematics of the control points on the top rear wing.

2.2 BITE-Wing CFD simulation

In order to gain insight into the thrust and lift production mechanisms in the BITE-Wing, a computational study of the unsteady flow over this vehicle was performed. The flow solver employed, called *feflo*, is based on simple finite elements. This flow solver has been employed to study several flapping flight configurations, such as the Drosophila fruit fly in hovering flight (Ramamurti and Sandberg, 2002)[9] and the aquatic flight of a Bird-wrasse fish (Ramamurti *et al*, 2002)[10]. Ramamaurti and Sandberg (2002)[9] have conducted studies on mesh refinement and the effect of viscosity. They showed that the effect of viscosity was minimal and that the lift forces were dominated by the translational and rotational effects. Also, guided by that experience we employ a grid that containing 570k points and 3·2m tetrahedral elements.

The kinematics of the biplane wings was obtained from experimental data. The BITE-Wing was clamped in a fixed position, facing into airflow of approximately 7·5ft/sec, the measured cruise speed of the vehicle. Four luminescent markers, shown in Fig. 2, were placed on each of the wings. The locations of the markers were selected our experience with the study on the Bird-wrasse fin. The markers were placed at a constant spanwise location, the first marker at the leading edge, the second 1·0cm behind the leading edge, the third at mid-chord, and the last on the trailing edge of the wing. The motion of the wings was captured using a Canadian Photonics Laboratory MS10K-CCD high-speed digital camera at a frame rate of 200Hz. The captured images were then digitised to obtain the unsteady kinematics of the wings. The digitised data were averaged over two cycles of flapping oscillation. Figure 3 shows the cross sectional shape of the top wing of the rear pair of biplanes for successive frames from the digitisation for a little over one period of the flapping cycle. Between frames t4 and t5 the leading edge of the wing has gone through the stroke reversal, but the trailing edge continues to move upward. This motion is clearly seen in Fig. 4, which shows the kinematics of the four selected points. This process is repeated to obtain the kinematics for all four wings.

Unsteady simulations were carried out for the top wing of the rear pair of wings for several cycles of wing oscillation. In this computation only the top wing is considered. The time period for the flapping oscillation is 0·1075sec and the forward velocity of the wing was set to be 7·5ft/sec. The Reynolds number (Re) based on this inflow velocity and the chord of the back wing at rest is approximately 10,800. Therefore, the flow is laminar and as a first approximation unsteady simulations using the Euler equations were computed. The time-varying lift and thrust forces were obtained by integrating the surface pressure distribution. Figure 5 shows the variation of the forces during two consecutive cycles. It is clear that a limit cycle has been reached. During the closing portion of the cycle, downstroke, the lift force reaches a peak value of 0·0623lbs.

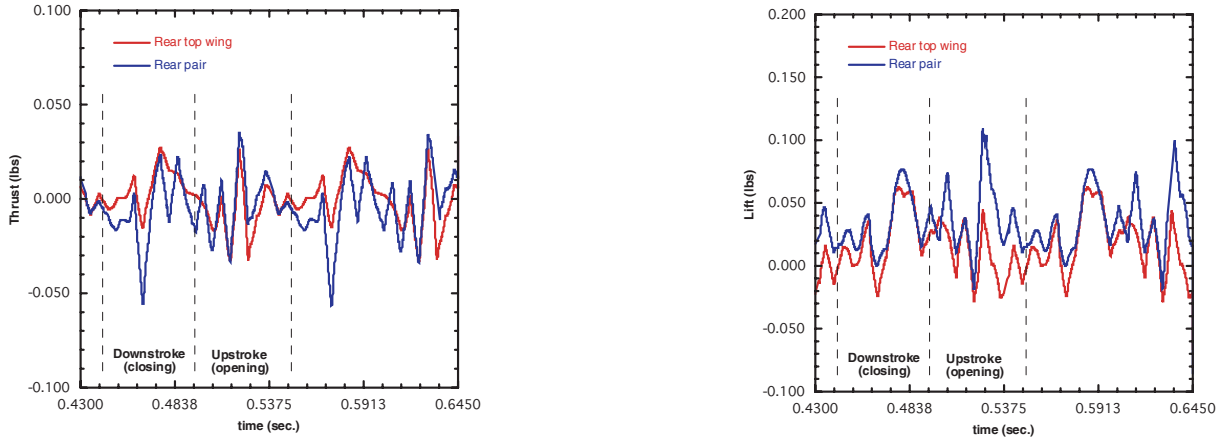


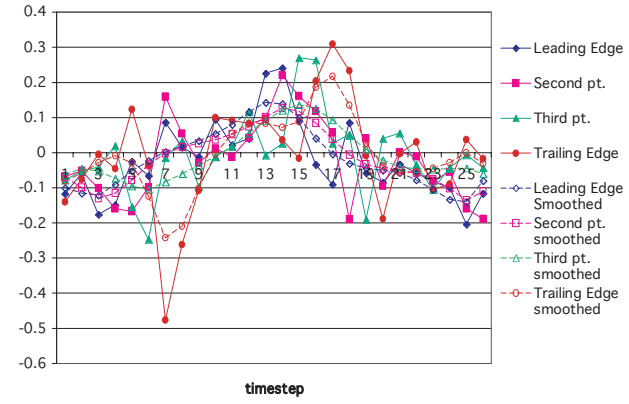
Figure 5. Thrust and lift production from the rear top wing and the rear pair of wings.

https://doi.org/10.1017/S0001924000000786 Published online by Cambridge University Press

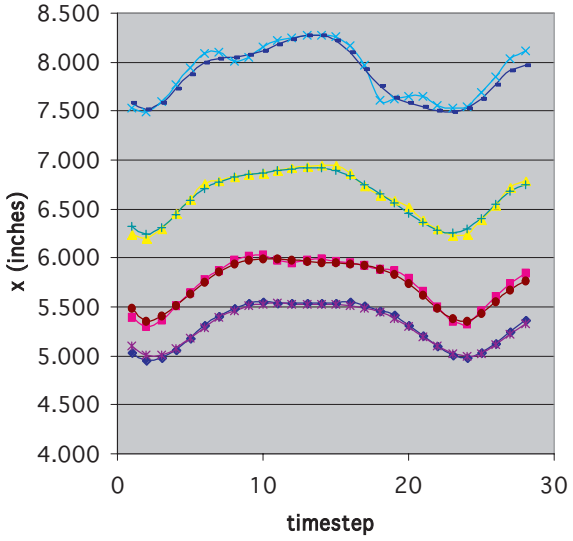
and the thrust 0·027lb from the top rear wing alone. The mean thrust force is nearly zero, implying that the vehicle with just the top rear wing will be able to maintain the forward velocity. The mean lift is approximately 0·0344lb. During the downstroke, the pair when compared to the top wing flapping alone produces more drag, and the thrust production during the upstroke is nearly unchanged by the addition of the lower wing. The lift during the upstroke is almost doubled when compared to the single wing and is nearly unchanged during the downstroke.

During the upstroke, both lift and thrust forces experience two reversals in the direction of the forces. The reason for this change may arise from the kinematics of the prescribed motion. This behavior was traced to a similar trend in the acceleration of the control points that was used to prescribe the kinematics. Figure 6(a) shows the vertical acceleration of all the four control points on the top rear wing. Although the motion of these control points, shown in Fig. 4, is relatively smooth, the acceleration exhibits a few reversal in both up and downstrokes. The reason for this could be errors in the digitisation process. Therefore, the acceleration of these control points are smoothed, shown in the dotted lines, and integrated twice to obtain a smoothed kinematics. Figure 6(b) and 6(c) show the coordinates of the control points before and after smoothing the acceleration. Similar smoothing operations were performed for all the other wings.

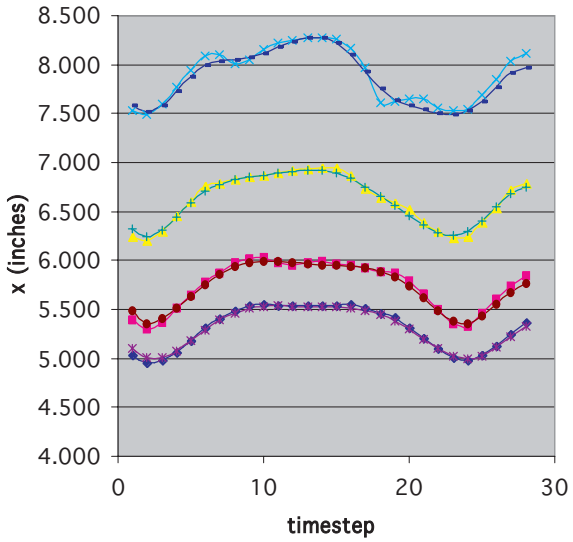
Next, unsteady simulations were performed with the front pair of wings added. Using the raw kinematics, the time history of the forces obtained from the unsteady flow simulation is shown in Fig. 7. A net drag of 0·045lb is produced by this configuration. The mean drag produced by the front pair is approximately 0·03lb and that produced by the back pair of wings is 0·015lb. The mean lift produced by the front and back pair of wings is 0·0173lb and 0·0264lb respectively. The total mean lift produced by this configuration is 0·0437lb (19·9 grams), which is approximately the weight of the vehicle (20g). The time history of the forces show several reversals during both up and down strokes. The force time history using the smoothed kinematics is shown in Fig. 8. It is clear that the higher frequencies in the force time history is due to the errors in the kinematics of the control points. The thrust reaches a peak of 0·004lb during the downstroke and a value of 0·0158lb during the upstroke, with a net drag of 0·0056lb during the cycle. Also, most of the total thrust is produced by the rear pair of wings and the contribution from the front pair contributes is a net drag. The lift reaches a peak value of 0·057lb at 0·253sec. during the downstroke, and 0·05lb at two instants, 0·3sec. and 0·33sec, during the upstroke. Figure 9 shows the surface pressure distribution at 0·3sec. and 0·33sec. It can be seen that the major contribution to the lift comes from the lower rear wing at 0·3sec. and from the upper front wing at 0·33sec. In order to understand the origin of the peak forces, the pressure distribution on the symmetry plane is plotted in Fig. 10. At t = 0·252sec, Fig. 10(a), more than half the lift is produced by the rear pair. At this instant, the top wing of the front pair produces a large lift that is offset by the bottom wing. The thrust produced by the front pair is nearly zero as the force vector is aligned with the y-direction and the thrust produced by the top rear wing is offset by the bottom wing. At t = 0·3sec, Fig. 10(b), more than 80% of the total lift contribution comes from the rear pair of wings, with a major contribution from the bottom wing. The second lift peak during the upstroke occurs at t = 0·33sec. Figure 11(a) shows that this lift is produced mainly by the upper wing of the front pair. At this instant, we can also see that a leading edge vortex (LEV), Fig. 11(b), separates from the top surface of the upper front wing. Also, it can be seen that a LEV shed from the previous stroke has just reached the leading edge of the upper rear wing. At this instant the lift contribution from the rear pair of wings shows a small increase, which could be due to the wake capture of this shed LEV. In order to maximise this effect, the length of the beam and the pitch orientation of the vehicle have to be adjusted so that the top rear wing passes through this vortex at the appropriate angle-of-attack.



(a) acceleration



(b) x-co-ordinate



(c) y-co-ordinate

Figure 6. Modified kinematics of the top rear wing.

https://doi.org/10.1017/S0001924000000786 Published online by Cambridge University Press

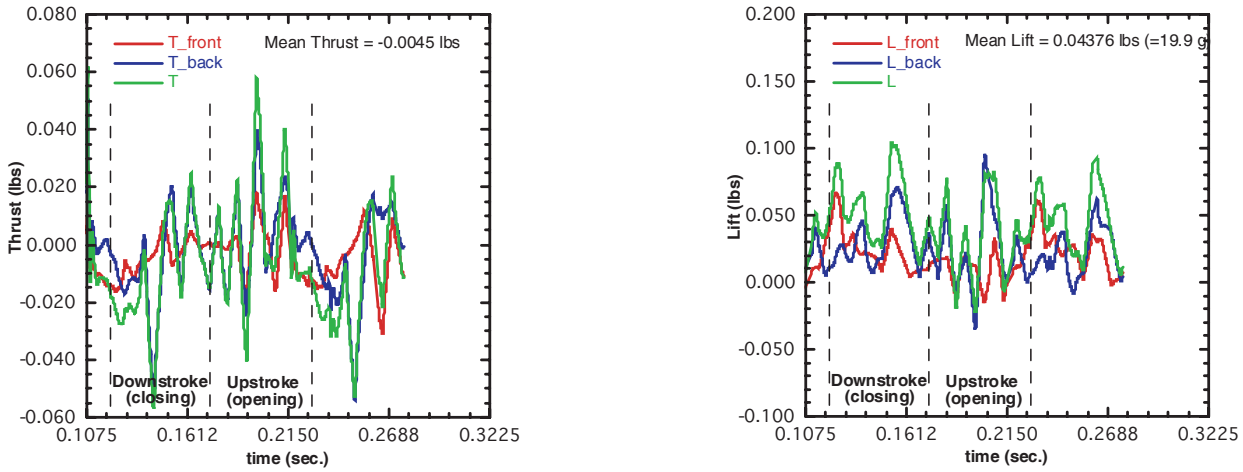


Figure 7. Thrust and lift production of the BITE wing with raw kinematics.

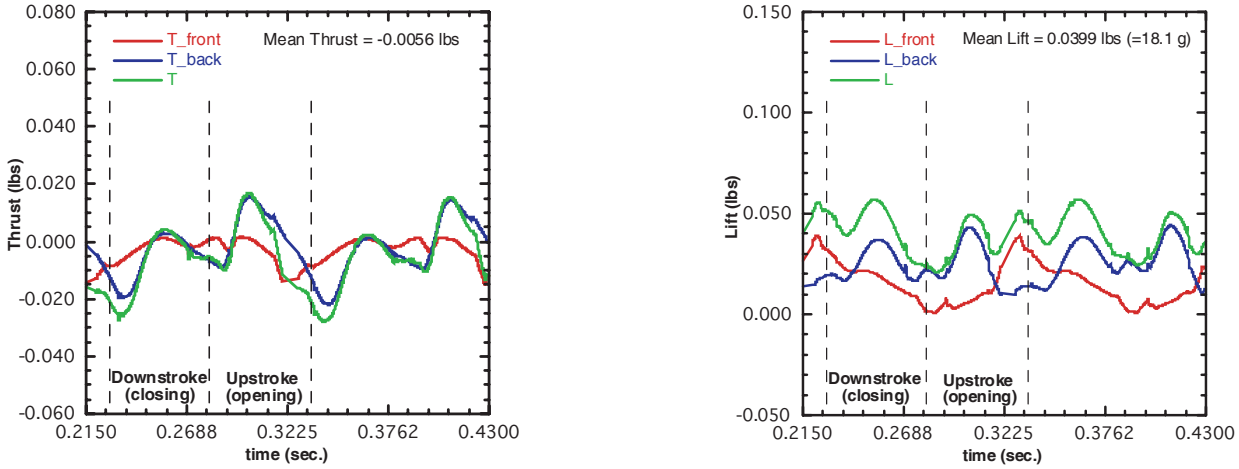
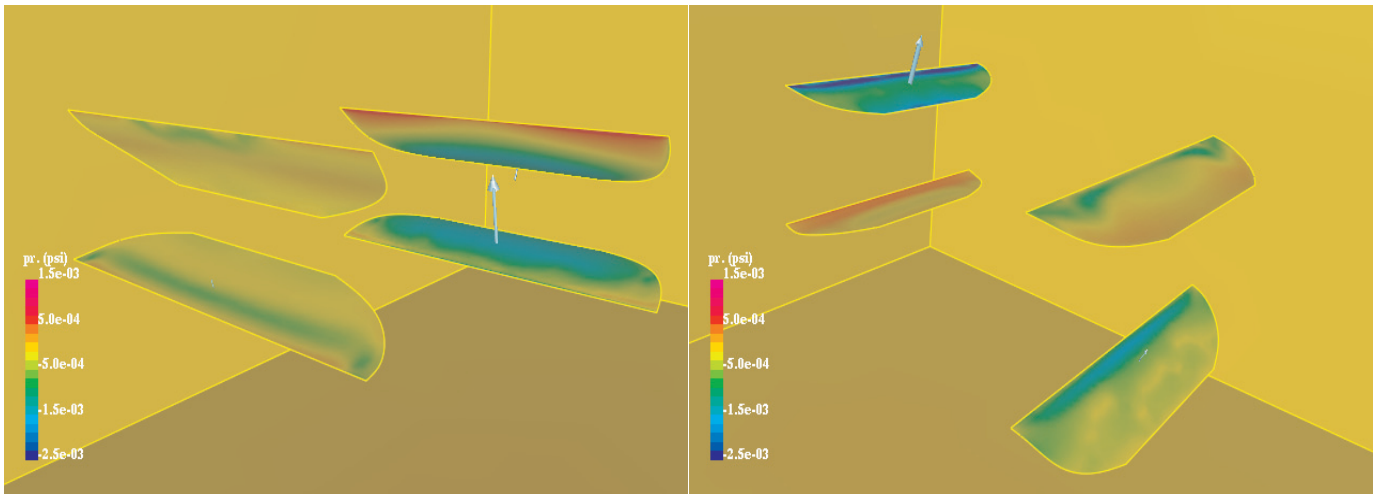


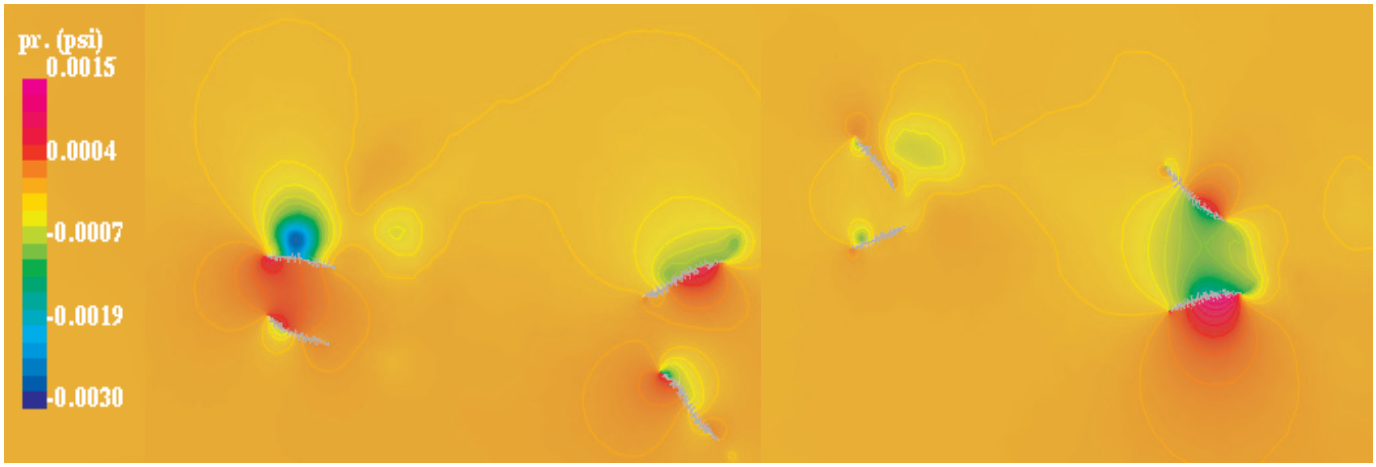
Figure 8. Thrust and lift production of the BITE wing with smoothed kinematics.



(a) $t = 0{\cdot}3$sec (b) $t = 0{\cdot}33$sec

Figure 9. Surface pressure distribution showing dominant force vectors at maximum lift condition during upstroke.

https://doi.org/10.1017/S0001924000000786 Published online by Cambridge University Press



(a) t = 0·252sec (b) t = 0·3sec

Figure 10. Pressure contours on the symmetry plane at peak lift production instants.

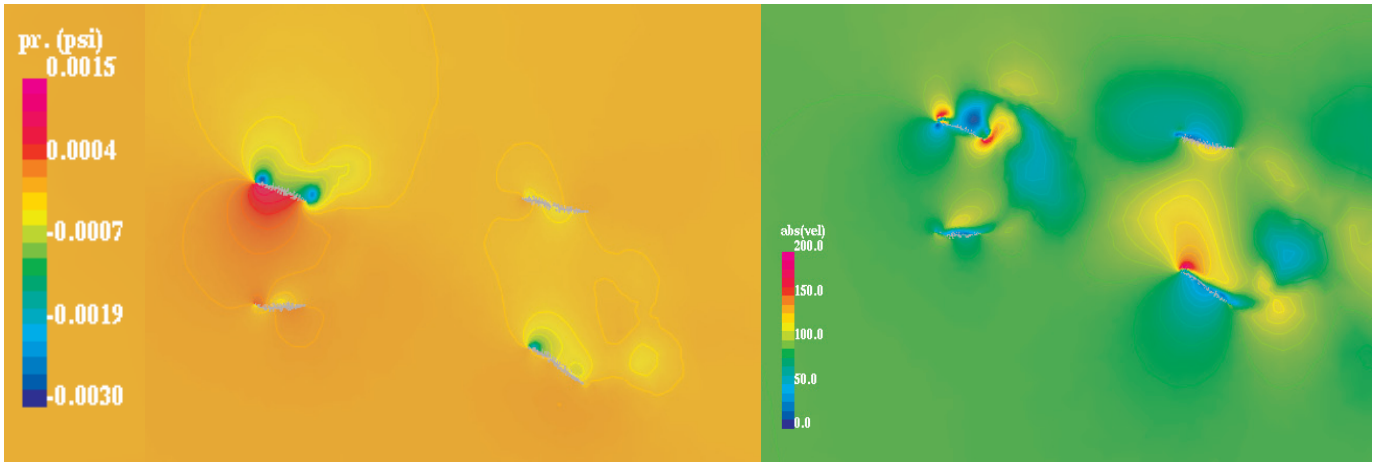


Figure 11. Pressure and magnitude of velocity contours on the symmetry plane at t = 0·33sec.

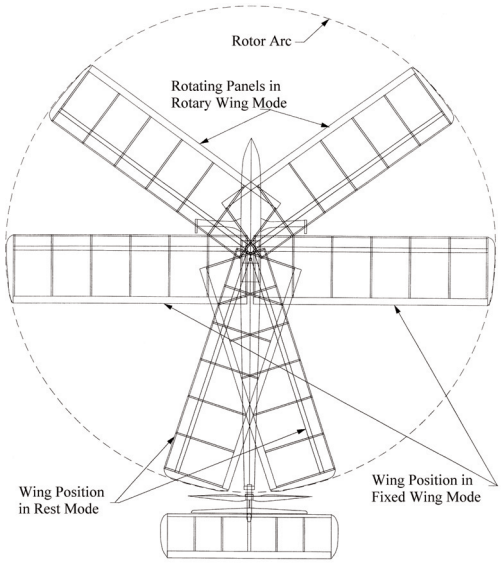




Figure 12. Two views of a radio-controlled Samara MAV configuration showing the position of the wing panels in different modes of operation.

https://doi.org/10.1017/S0001924000000786 Published online by Cambridge University Press

4.0 STOP-ROTOR MAV: SAMARA

Interest in an MAV that can land or 'perch' in remote locations and then take to the air again has led to the development of a novel stop-rotor configuration, the 'Samara', which takes its name from the family of rotating winged plant seeds, e.g. the maple seed. In this vehicle we hope to capture some of the locomotion capabilities of the grasshopper: vertical or near vertical takeoff and landing, low speed flight with agile maneuvering, and efficient high-speed flight.

The Samara employs a pair of single-blade, rotary/fixed wing panels, attached at the roots to separate coaxial shafts. There is a slight vertical separation between the panels. The wings operate in three modes: rotary, fixed, and rest (see Fig. 12(a)). Rotary wing mode is used for vertical or near vertical takeoff and landing and agile low-speed flight. The contra-rotating panels are mechanically linked to turn at the same speed and to maintain their relative rotational phasing. The two panels always maintain mirror-image positions across the centerline of the aircraft. Their slight vertical separation prevents them from interfering with each other. A pusher propeller provides thrust and creates airflow over a set of conventional tail surfaces for control.

In fixed wing mode the panels are locked in place opposite each other, forming a conventional fixed wing except for their slight vertical displacement. This mode, in which the Samara is configured as an aeroplane, allows efficient high-speed flight over long ranges. Other stop-rotor converting aircraft use a wing assembly that rotates on the aircraft centerline as a conventional (single rotation direction) two-bladed rotary wing. The airflow over one of the wing/rotor panels must reverse direction when the rotor is stopped in flight for conversion to fixed wing mode. The pitch of these panels must also be changed to meet the airflow correctly when they are switched between rotary and fixed wing duty. This function requires a complex mechanism. It also requires the wing/rotor panels to use an airfoil that is symmetrical across the chord; it cannot have a preferred leading or trailing edge. Such airfoils are inefficient in comparison to single flow direction airfoils, both for fixed and rotary wings.

While on the ground the Samara enters rest mode, in which both wing panels are rotated back over the rear of the vehicle, eclipsing each other. The panels are lightweight, with a low moment of inertia, making it possible to start and stop wing rotation rapidly. This also mitigates the inherent problem, in rotary wing flight, of fore and aft vibration caused by the oscillatory shift in weight as the panels contra rotate. The mass of the wing panels is considerably less than the total vehicle mass. As an MAV of a few hundred grams weight, the Samara is not greatly affected by this inherent vibration. In a large aircraft, where the wing is a significant fraction of the vehicle mass, such a vibration would be catastrophic.

Two separate power plants are used to drive the pusher propeller and the rotors in different flight regimes. The main power plant has a transmission that can be switched to drive either wing rotation in rotary mode, or the propeller in fixed wing mode. The auxiliary power plant drives only the propeller. In rotary wing mode the auxiliary provides forward thrust while the main provides rotary lift, allowing fully independent power controls of both functions. When entering fixed wing mode, the main power plant shifts power from the rotors to the propeller, providing most of the thrust for high speed fixed wing flight. The auxiliary power plant is linked to the main to augment thrust.

Samara flight tests began with a free flight model, electrically powered, weighing 11·5grams. This model has flown successfully in both rotary and fixed wing modes. As it was not designed for in-flight conversion, the model had to be trimmed manually for stable flight in each mode. This model also lacked independent control for rotor and propeller speeds. Development is continuing with a 300gram radio controlled (RC) Samara (see figure 12(b)), on which the full range of intended design features will be tested. This aircraft includes two independently controlled electric motors, one of 40 watts capacity for the main rotor and a 7-watt auxiliary motor for the pusher propeller. It also has elevator and rudder control. Power is supplied by a 9·6 volt nickel cadmium battery pack. The RC Samara has made a number of vertical takeoff hops, and sustained forward flight in rotary wing mode was achieved in January 2003.

The stability and control requirements of the Samara are not fully known, but they may well be formidable. Development has taken a 'simplest first' approach; the current RC version has a rigid rotor system with no cyclic pitch control, and no independent roll control system. As the flight characteristics of the RC Samara are learned, additional control mechanisms will be added as necessary.

In order to understand the flight characteristics of this vehicle, computational simulations over the rotor were conducted. First, steady state flow over the Samara with the wing panels at different positions during one cycle of rotation was computed. A set of quasi-steady computations were carried out, as an intermediate step, to determine the differences between steady state computations for the wing panels at different positions during the rotation. To simulate the quasi-steady state solution at any instant of time, the rotational velocity of the rotor is imposed as the mesh velocity at the surface without actually moving the surface. Together with the incoming flow velocity the wing panels will be subjected to the proper angle-of-attack. The steady and quasi-steady results are shown in Fig. 13. Comparing the thrust (force in the -ve x-direction), we see that the steady state results produce a drag for positions of the wings between 90° and 270° , whereas the quasi-steady state results show a net thrust produced in this phase. The lift production from the steady and quasi-steady results on the other hand shows a large discrepancy in both magnitude and trend. The pitching moment, Fig. 13(b), shows that the quasi-steady results produce a large negative moment when the wing panels are at 45° compared to the steady results. Comparison of the surface pressure distribution at this position, Fig. 14, shows that both magnitude and the distribution of pressure are very different between the two results. The pressure distribution on a plane midway between the two wing panels, Fig. 15, also confirms this. Our earlier computations on a swimming Bird-wrasse (Ramamurti *et al*, 2002)[10] the steady state results were found to be insufficient in predicting the forces and the quasi-steady results are useful in determining the trends and do not, however, provide accurate estimates in the magnitude of forces. Hence, a completely unsteady computation of the rotating wing panels is performed.

Figure 16 shows the time history of forces and moments of a Samara flying at 15ft/s with its wing panels rotating at 540rpm using the unsteady remeshing flow solver described in this paper. We can see that a small drag force and almost zero sideways force are developed, as would be expected. The lift force shows a similar trend that was predicted by the quasi-steady results, but the maximum lift produced in the first cycle of rotation is approximately 1·2lb compared to 0·4lb predicted by quasi-steady simulation. Also, the quasi-steady simulations do not predict the precipitous drop in the lift around 90° of rotation of the wing panels. The pitching moment from the unsteady simulation reaches a peak negative value of –0·8ft-lb near 90° of rotation, whereas the quasi-steady results predict a value 0f –0·12ft-lb at 45° of rotation. The pressure distribution on the plane midway between the two panels after 45° of rotation, Fig. 17, shows the center of the low pressure region on the bottom of the wing is situated nearly 75% of span away from the center of rotation which is not predicted by both the steady and quasi-steady state results. Also, the magnitude of pressure predicted by the unsteady simulation is almost five fold higher. In order to understand the drop in lift around 90° of rotation, the pressure distribution on the panels are plotted and are shown in Fig. 18. At this instant, the top panel produces a negative lift of approximately 0·22lb while the lower panel produces a positive lift of 0·44lbs. From Fig. 18(b), we can see that a large low pressure region exists on the lower surface of the upper panel resulting in the loss of lift. This is due to the fact that this panel is cutting through the high velocity fluid flowing over the upper surface of the lower panel, which is opposite to the direction of rotation of the top panel. The high pressure on the bottom surface of the lower panel in the outer half of the wing leads to the positive lift.

https://doi.org/10.1017/S0001924000000786 Published online by Cambridge University Press

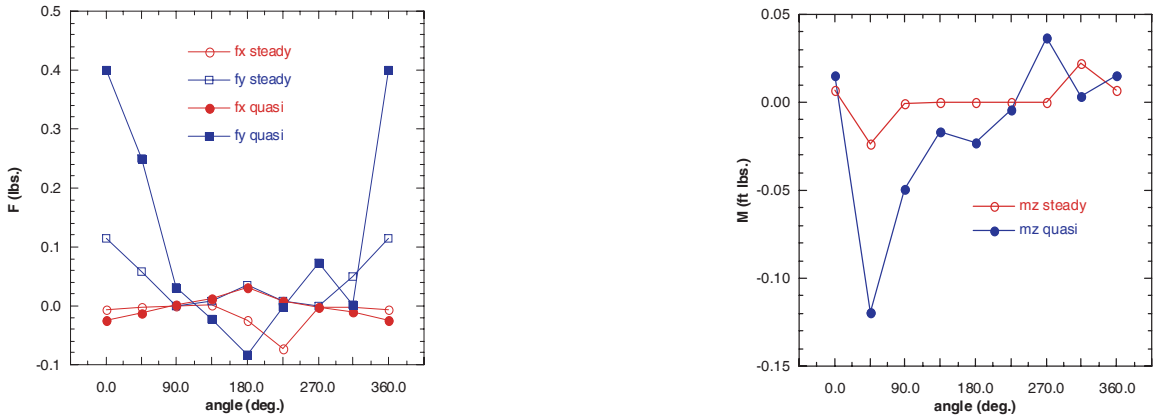


Figure 13. Steady and quasi-steady state thrust, lift and pitching moment on the Samara for various positions of the wing.

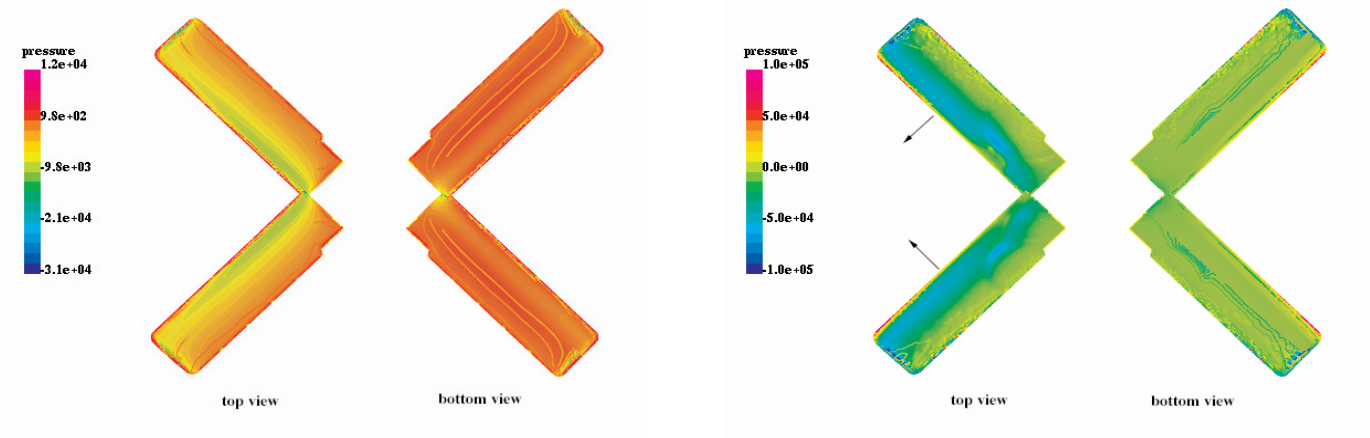


Figure 14. Surface pressure distribution on the Samara wing panels oriented at 45°.

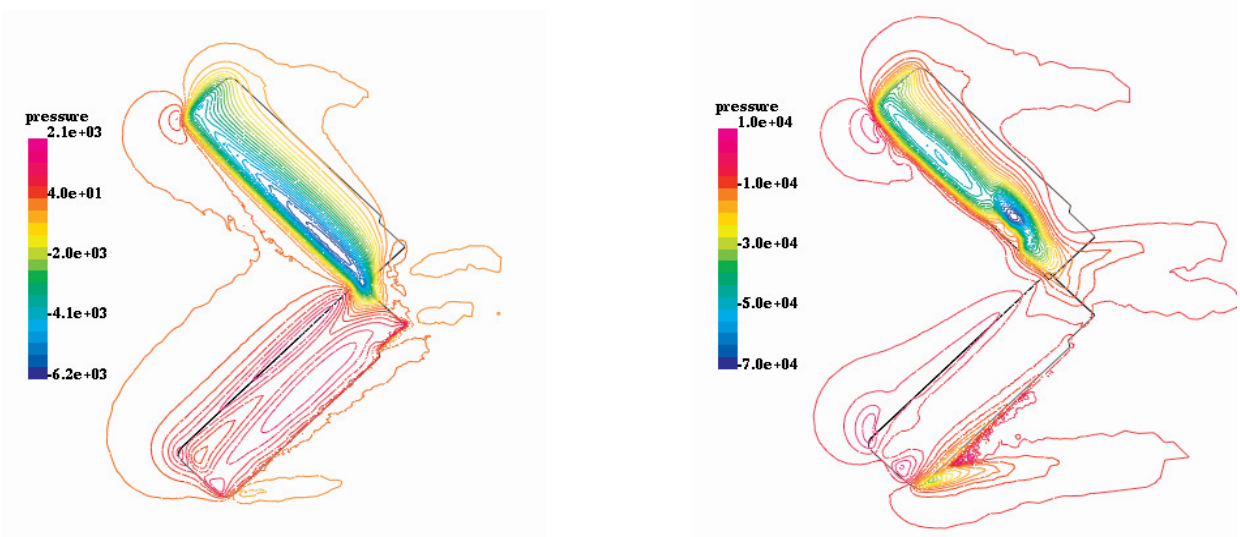


Figure 15. Pressure distribution on a plane midway between the two wing panels.

https://doi.org/10.1017/S0001924000000786 Published online by Cambridge University Press

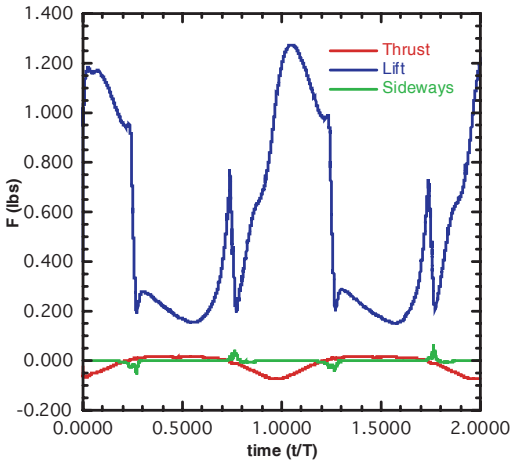


Figure 16. Force and moment time histories for rotating Samara, ω = 540rpm, V = 15ft/s.

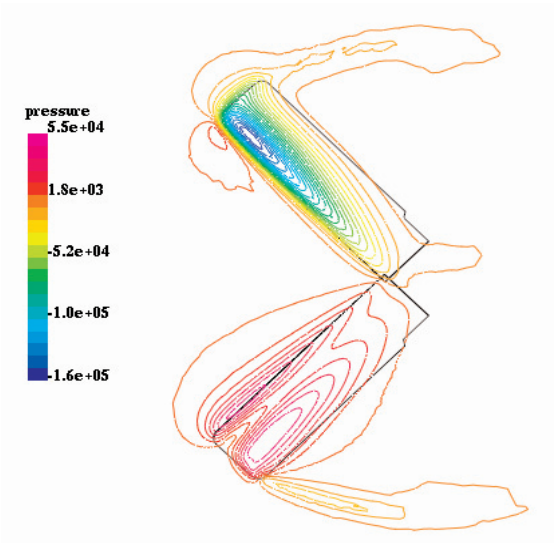


Figure 17. Pressure distribution on a plane midway between the two panels after 45° of rotation.

5.0 CONCLUSION

The reversing-camber flapping wing has proven to be a versatile mechanism for producing thrust/lift in low Reynolds number conditions. The BITE-Wing configuration employs four reversing-camber flapping wings eliminating the need for fixed wings entirely. Several principles of insect locomotion apply or may apply to the BITE-Wing. It uses tandem flapping wings with no fixed surfaces, like the dragonfly. Computational studies showed that the digitisation errors in obtaining the kinematics of the flapping wings can result in force time histories wherein there are several reversals of forces during both up and downstrokes. This can be eliminated by smoothing the kinematics based on the acceleration of the control points. This configuration is amenable to some form of vortex capture, as seen in the fruit fly and other two-winged insects.

The unsteady computations of the Samara are compared with quasi-steady state computations. We found that the quasi-steady state computations with the velocity of the wing properly superimposed was useful in predicting the trends in the force time history but incapable of providing accurate estimates of force production. The unsteady results showed that the Samara loses lift when the two wing panels overlap, mainly due to the loss of lift in the upper panel. The pitching moment for this vehicle changes rapidly during one cycle of revolution. The computed flight characteristics will be used to better optimise the stability and control of this vehicle.

ACKNOWLEDGEMENTS

This work was supported by the Office of Naval Research through the Tactical Electronic Warfare Division Micro Air Vehicles Program of the Naval Research Laboratory, Washington DC, USA.

REFERENCES

1. DICKINSON, M.H., LEHMANN, F. and SANE, S.P. Wing rotation and the aerodynamic basis of insect flight, *Science*, June 1999, **284**, pp 1954-1960.
2. ELLINGTON, C.P. The aerodynamics of hovering insect flight, IV, *Aerodynamic Mechanisms*, Phil Trans. R Soc Lond B 1984, **305**, pp 79-113.
3. JONES, K.D. and PLATZER, M.F. Experimental investigation of the aerodynamic characteristics of flapping-wing micro air vehicles, AIAA (2003-0418), 2003.
4. KELLOGG, J., BOVAIS, C., CYLINDER, D., DAHLBERG, J. FOCH, R., PLATZER, M., RAMAMURTI, R. and SANDBERG, W.C. Non conventional aerodynamics for micro-UAVs, Proc 16th International UAV Systems Conference, April 2001, Bristol, UK.
5. KELLOGG, J., BOVAIS, C., FOCH, R., CYLINDER, D., RAMAMURTI, R., SANDBERG, W.C., GARDNER, J., SRULL, D., PIPER, G. and VAIANA, P. Development and testing of unconventional micro air vehicle configurations, AIAA Paper No 2003-6356.
6. RAMAMURTI, R. and LÖHNER, R. Evaluation of an Incompressible Flow Solver Based on Simple Elements, *Advances in Finite Element Analysis in Fluid Dynamics*, 1992, **137**, DHAUBHADEL, M.N. *et al* (Eds), ASME Publication, New York, pp 33-42.
7. RAMAMURTI, R., LÖHNER, R. and SANDBERG, W.C. Evaluation of a scalable 3-D incompressible finite element flow solver, AIAA Paper No 94-0756, 1994.
8. RAMAMURTI, R., LÖHNER, R. and SANDBERG, W.C. Simulation of a torpedo launch using a 3-D incompressible finite element flow Solver, AIAA Paper No 95-0086, 1995.
9. RAMAMURTI, R. and SANDBERG, W.C. A 3-D computational study of the aerodynamic characteristics of insect flight, *J Exp Biology*, May 2002, **205**, (10), pp 1507-1518.
10. RAMAMURTI, R., SANDBERG, W.C., LÖHNER, R., WALKER, J.A. and WESTNEAT, M.M. Fluid dynamics of flapping aquatic flight in the bird wrasse: 3-D unsteady computations with fin deformation, *J Exp Biology*, October 2002, **205**, (19), pp 2997-3008.

https://doi.org/10.1017/S0001924000000786 Published online by Cambridge University Press

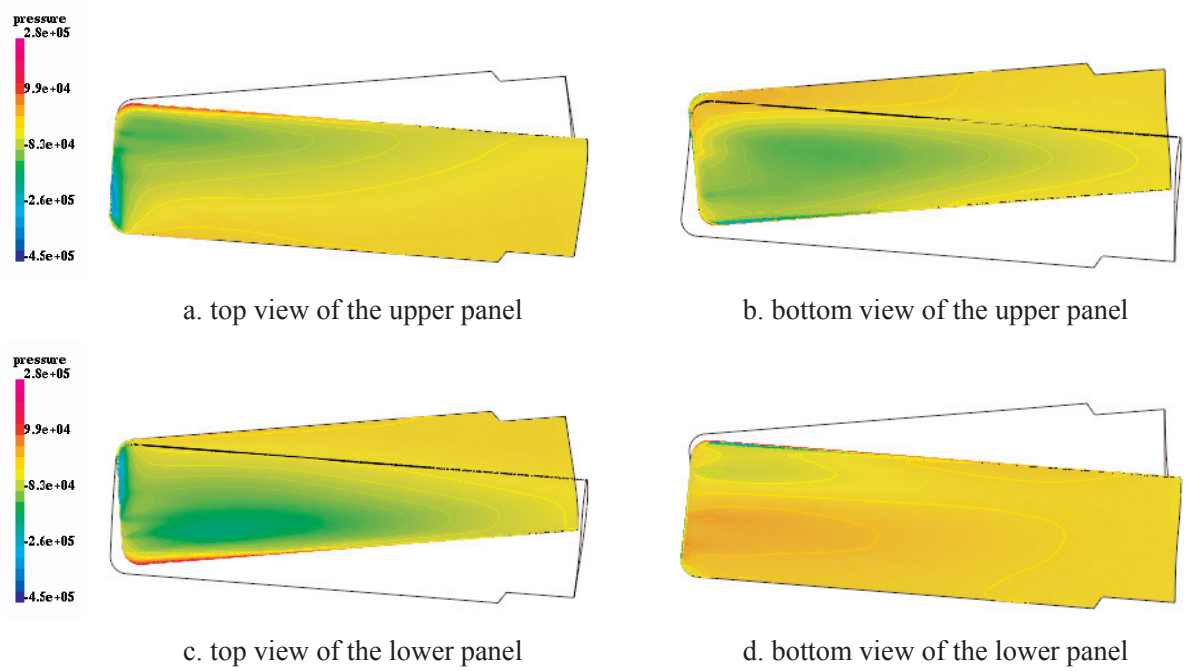


Figure 18. Surface pressure distribution on the Samara wing panels just after 90° rotation, $t = 0{\cdot}0292$ sec.

https://doi.org/10.1017/S0001924000000786 Published online by Cambridge University Press